



# Combinatorial laser molecular beam epitaxy system integrated with specialized low-temperature scanning tunneling microscopy

Cite as: Rev. Sci. Instrum. **91**, 013904 (2020); <https://doi.org/10.1063/1.5119686>

Submitted: 11 July 2019 . Accepted: 19 December 2019 . Published Online: 09 January 2020

Ge He , Zhongxu Wei, Zhongpei Feng, Xiaodong Yu, Beiyi Zhu, Li Liu, Kui Jin , Jie Yuan, and Qing Huan



View Online



Export Citation



CrossMark

## ARTICLES YOU MAY BE INTERESTED IN

[1 fm/ \$\sqrt{\text{Hz}}\$  noise level low temperature Fabry-Pérot atomic force/magnetic force microscope operating in 4–300 K temperature range](#)

Review of Scientific Instruments **91**, 013703 (2020); <https://doi.org/10.1063/1.5120007>

[A compact electron cyclotron resonance negative hydrogen ion source for evaluation of plasma electrode materials](#)

Review of Scientific Instruments **91**, 013508 (2020); <https://doi.org/10.1063/1.5128610>

[High-stability, high-voltage power supplies for use with multi-reflection time-of-flight mass spectrographs](#)

Review of Scientific Instruments **91**, 014702 (2020); <https://doi.org/10.1063/1.5104292>



## VACUUM SOLUTIONS FROM A SINGLE SOURCE

Pfeiffer Vacuum stands for innovative and custom vacuum solutions worldwide, technological perfection, competent advice and reliable service.

[Learn more!](#)

# Combinatorial laser molecular beam epitaxy system integrated with specialized low-temperature scanning tunneling microscopy

Cite as: Rev. Sci. Instrum. 91, 013904 (2020); doi: 10.1063/1.5119686

Submitted: 11 July 2019 • Accepted: 19 December 2019 •

Published Online: 9 January 2020



View Online



Export Citation



CrossMark

Ge He,<sup>1,2</sup>  Zhongxu Wei,<sup>1,2</sup> Zhongpei Feng,<sup>1,2,3</sup> Xiaodong Yu,<sup>1,2</sup> Beiyi Zhu,<sup>1</sup> Li Liu,<sup>1</sup> Kui Jin,<sup>1,2,3,4,a)</sup>  Jie Yuan,<sup>1,3,4,a)</sup> and Qing Huan<sup>1,3,4,5,a)</sup>

## AFFILIATIONS

<sup>1</sup>Beijing National Laboratory for Condensed Matter Physics, Institute of Physics, Chinese Academy of Sciences, Beijing 100190, China

<sup>2</sup>School of Physical Sciences, University of Chinese Academy of Sciences, Beijing 100049, China

<sup>3</sup>Songshan Lake Materials Laboratory, Dongguan, Guangdong 523808, China

<sup>4</sup>Key Laboratory for Vacuum Physics, University of Chinese Academy of Sciences, Beijing 100190, China

<sup>5</sup>CAS Center for Excellence in Topological Quantum Computation, University of Chinese Academy of Sciences, Beijing 100190, China

<sup>a)</sup>Authors to whom correspondence should be addressed: [kuijin@iphy.ac.cn](mailto:kuijin@iphy.ac.cn); [yuanjie@iphy.ac.cn](mailto:yuanjie@iphy.ac.cn); and [huanq@iphy.ac.cn](mailto:huanq@iphy.ac.cn)

## ABSTRACT

We present a newly developed facility comprising a combinatorial laser molecular beam epitaxy system and an *in situ* scanning tunneling microscope (STM). This facility aims at accelerating the materials research in a highly efficient way by advanced high-throughput film synthesis techniques and subsequent fast characterization of surface morphology and electronic states. Compared with uniform films deposited by conventional methods, the so-called combinatorial thin films will be beneficial in determining the accurate phase diagrams of different materials due to the improved control of parameters such as chemical substitution and sample thickness resulting from a rotary-mask method. A specially designed STM working under low-temperature and ultrahigh vacuum conditions is optimized for the characterization of combinatorial thin films in an XY coarse motion range of 15 mm × 15 mm with submicrometer location precision. The overall configuration and some key aspects such as the sample holder design, scanner head, and sample/tip/target transfer mechanism are described in detail. The performance of the device is demonstrated by synthesizing high-quality superconducting FeSe thin films with gradient thickness and imaging surfaces of highly oriented pyrolytic graphite, Au (111), Bi<sub>2</sub>Sr<sub>2</sub>CaCu<sub>2</sub>O<sub>8+δ</sub> (BSCCO), and FeSe. In addition, we also have obtained clean noise spectra of tunneling junctions and the superconducting energy gap of BSCCO. The successful manufacturing of such a facility opens a new window for the next generation equipment designed for experimental materials research.

Published under license by AIP Publishing. <https://doi.org/10.1063/1.5119686>

## I. INTRODUCTION

The emergence of exotic electronic states relies on an exact control of physical parameters, both in synthesis and manipulation.<sup>1–4</sup> For instance, giant magnetoresistance emerges in multilayers composed of alternating ferromagnetic and nonmagnetic conductive

layers.<sup>1</sup> By doping a Mott insulator, the electronic state evolves from an insulating state to a high- $T_c$  superconducting state and then to Fermi liquid regime, along with various ordered states or fluctuations.<sup>2–4</sup> Accurate and unified phase diagrams of the materials will be beneficial both for the comprehension of basic physical concepts and their applications. However, traditional methods for

exploring new materials are becoming inefficient in view of the rapidly growing demands from various fields. To obtain a complete doping-dependent phase diagram by the conventional one-at-a-time strategy, one must synthesize and characterize samples one doping level after another.<sup>3,5,6</sup> As the number of elements in the compounds increases, the workload increases geometrically. As a result, it is nearly impossible to establish a precise phase diagram for compounds comprised of multiple elements. Moreover, it is hard to pin down critical chemical compositions such as quantum critical points (QCPs), which are important for the understanding of competing orders in condensed matter.<sup>7-9</sup> Therefore, developing new technologies with both high-efficient synthesis and characterization becomes vital for materials science.

The combinatorial method first introduced by Hanak supplies a high-throughput approach to synthesize samples efficiently.<sup>10</sup> This technique has shown significant advantages for exploring new materials<sup>11</sup> and investigating their physical properties.<sup>12</sup> Up to now, the combinatorial film (combi-film) deposition technique has been through three generations:<sup>13</sup> cosputtering or coevaporation,<sup>14</sup> array mask technique,<sup>15,16</sup> and combinatorial laser molecular beam epitaxy (Combi-LMBE).<sup>17</sup> Overcoming the drawbacks of nonlinear and uncontrollable composition gradients in the first- and the discrete stoichiometric ratio in second-generation techniques, Combi-LMBE technique could provide one- or two-dimensional composition-spread films by a horizontal mobile mask system. Most established Combi-LMBE systems use reciprocating motion of the mask by a precisely controlled motor.<sup>17,18</sup> In this case, the method induces an accumulative error that eventually has an impact on the accuracy of the composition. In addition, repeated forward and backward operations of the mask will result in the deformation of mechanical components. Clearly, alternative methods realize that the composition gradients are needed to overcome the drawbacks mentioned above.

Besides the challenges in synthesis, the lack of proper characterization tools for the combi-film severely limits the wide applications of the high-throughput methods in materials research, where a probe with high spatial resolution is necessary. There are some commercial instruments available, e.g., wavelength dispersive spectroscope (WDS),<sup>19</sup> x-ray fluorescence spectroscope (XFS),<sup>20</sup> and x-ray diffractometer,<sup>21,22</sup> for characterization of the structure and component, fluorescence spectroscopy<sup>23</sup> and transmission spectroscopy,<sup>24</sup> and for inspecting optical properties. In addition, some laboratory devices suitable for the combi-films have been developed, such as the scanning superconducting quantum interference device (SSQUID)<sup>25</sup> and scanning Hall microscope<sup>26,27</sup> to detect weak magnetic signals, scanning near-field microwave microscope<sup>28-30</sup> to characterize dielectric properties, and the spring probe array<sup>11,31</sup> to measure electrical transport properties. To our knowledge, there is still no report on the implementation of local probing of electronic states of combinatorial samples. Scanning tunneling microscopy/spectroscopy (STM/STS) has been widely used in the study of molecular vibration modes,<sup>32</sup> spin flip,<sup>33</sup> Kondo effect,<sup>34</sup> and superconductivity<sup>35</sup>. STM probing requires very clean surfaces, which can only be achieved by *in situ* ion bombing, annealing, or cleaving, but most of the combinatorial samples cannot satisfy such requirements. Besides, a large range horizontal positioning up to 10 mm × 10 mm in a high precision spatial resolution is required to match the merits of common combi-films. These specs are out

of range for most commercial and home-made STM systems with limited XY coarse motion (less than 5 mm) and not suitable for composition spreads.<sup>36-39</sup>

There are quite a few MBE-STM systems that have been implemented previously.<sup>40-42</sup> However, MBE is often used in uniform film deposition in these systems. One can obtain only one doping at one deposition. By contrast, Combi-LMBE is designed to deposit phase spread films in one or two dimensions. In addition, compared with conventional MBE systems, LMBE systems are good at growing oxide samples. Besides, the XY coarse motion of the sample stage in STM scanner heads of these systems is less than 5 mm and without precise positioning, which makes it unsuitable for combi-films characterization.

In this paper, we describe the design, the build, and the performance testing of a newly developed combined system of Combi-LMBE and low-temperature ultrahigh vacuum scanning tunneling microscopy (LT-UHV-STM). The system aims at synthesizing combi-films and characterizing their surface morphology and electronic states *in situ* with high efficiency and precision. Compared with the commercial Combi-LMBE system, we used a rotatable circular mask to avoid the accumulative error from reciprocating motion of the flat mask. Within the STM unit, we designed a scanner head with a large XY coarse motion range (15 mm × 15 mm) and a positioning resolution, which is better than 1 μm at liquid helium temperature. In order to test the performance of the system, we deposited the FeSe film with gradient thickness by utilizing the rotation mask. The thickness-gradient samples show high quality and nearly linear-in-position thickness ranging from 28 nm to 280 nm, with the superconducting transition temperature between 8 and 10 K. Besides, we obtained high-quality images of highly oriented pyrolytic graphite (HOPG), Au (111), Bi<sub>2</sub>Sr<sub>2</sub>CaCu<sub>2</sub>O<sub>8+δ</sub> (BSCCO), and FeSe surfaces and *dI/dV* spectra of BSCCO. The system exhibits good stability with respect to both combi-film deposition and STM measurements. Its features should prove especially advantageous in superconductivity research.

## II. SYSTEM DESIGN

### A. Ultrahigh vacuum chamber

Figure 1 shows a 3D model and a photograph of the system. The whole system with a weight of 1.6 ton is supported by a T-shape aluminum alloy frame with a cross section of 80 mm × 80 mm. Three pneumatic vibration isolators are located at the three terminal vertexes of the frame, respectively [see the black cylinders in Fig. 1(a)]. The estimated mass center of the system is shown by a red dot in Fig. 1(a). The system consists of six chambers, that is, Combi-LMBE chamber, radial telescopic transfer arm (RTTA) chamber (from Kurt J. Lesker Company), STM chamber, preparation chamber, load-lock chamber, and buffer chamber [see Figs. 1(a) and 1(b)]. The load-lock chamber is for loading samples, targets, and STM tips. The preparation chamber is installed with a customized manipulator (from UHV Design Ltd.) and an ion gun. Cycles of ion bombardment and annealing (up to 1200 °C) of the sample can be performed in this chamber. The details of the buffer chamber, the Combi-LMBE chamber, the RTTA chamber, and the STM chamber will be discussed below.

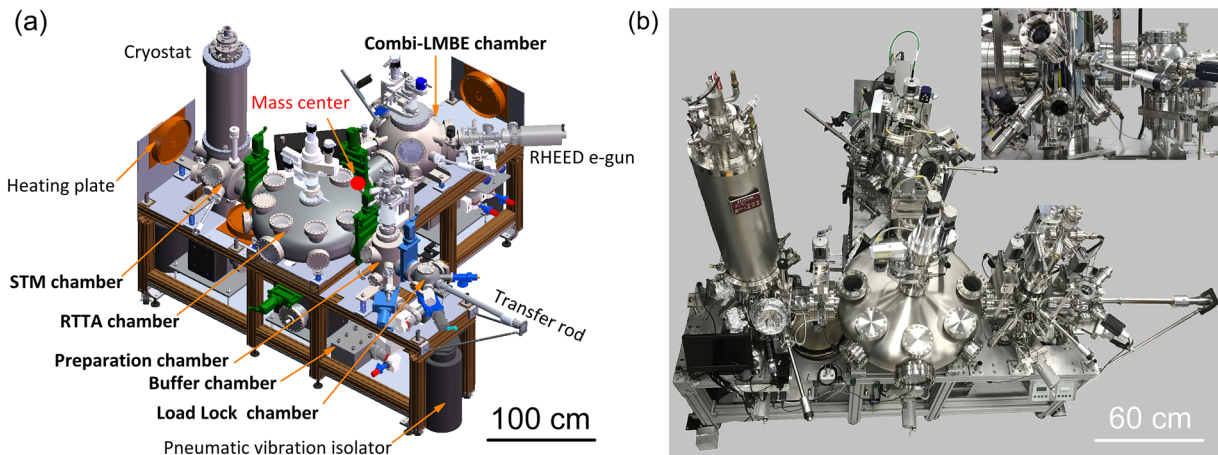


**FIG. 1.** 3D CAD drawing and photograph of the system. (a) Isometric view of the system. The chambers, transfer rod, vibration isolators, cryostat, RHEED, etc. are indicated in the figure. The red dot shows the mass center of the system. (b) Photograph of the system. The preparation chamber and the load-lock chamber are shown in the inset.

To obtain ultrahigh vacuum, a multilevel pump system is used including mechanical pumps, turbomolecular pumps, sputter-ion pumps, titanium-sublimation pumps (TSP), and nonevaporable getter (NEG) pumps. A 1600 l/s turbo-molecular pump is installed between the RTTA and the Combi-LMBE chambers, which pumps these two chambers as well as the STM chamber. Another 300 l/s turbomolecular pump, responsible for pumping the preparation and the load-lock chambers, is mounted under the preparation chamber. In order to reach a higher vacuum level, the outlet of these two turbomolecular pumps is connected to the buffer chamber with an 80 l/s turbomolecular pump and a 40 m<sup>3</sup>/h mechanical pump installed to achieve a vacuum better than 10<sup>-5</sup> Torr. When carrying out the STM characterization, all the turbomolecular pumps and mechanical pumps are turned off to minimize vibrations. Instead, the UHV environment is maintained by three ion pumps of 400 l/s

(integrated with TSP and Cryoshroud), 300 l/s (integrated with NEG), and 300 l/s (integrated with NEG), which are mounted under the Combi-LMBE chamber, the RTTA chamber, and the STM chamber, respectively. Three 5 kW heaters are used to bake the system [see the light brown colored round parts in Fig. 1(a)]. The whole system is covered by a home-designed heat-insulation tent during baking. The operating background pressure of the Combi-LMBE chamber, the RTTA chamber, and the STM chamber can easily be as low as ~10<sup>-10</sup> Torr after one week of baking at 130 °C.

## B. Transfer system

As described in Sec. II A, this is a complex system which has six chambers with multiple functions. Thus, it is crucial to carry out a reliable protocol for a smooth transfer of sample, substrate, tip, and

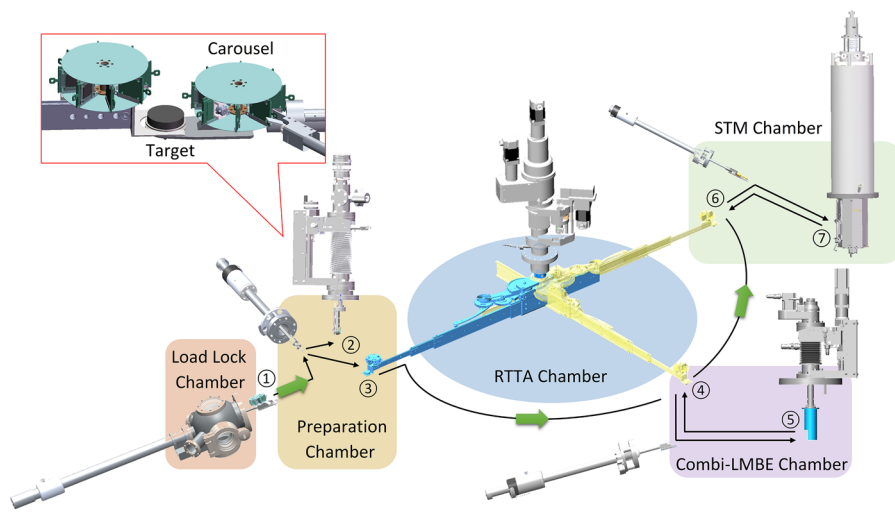


**FIG. 2.** Design of the sample transfer. The sample/substrate/target/tip is loaded from the load-lock chamber. Samples and tips can be transferred to preparation chamber by the transfer rod ①. A wobble stick mounted on the preparation chamber grabs the sample holder and places it to ② for ion sputtering and annealing. The sample/substrate/target/tip is transferred to RTTA at position ③. The target is transferred by a fork as shown in the inset. Then, the target is transferred from the RTTA chamber to the Combi-LMBE chamber ④ for deposition. The substrate is positioned at the sample stage ⑤. The samples and tips are transferred from RTTA ⑥ to the STM chamber ⑦ for characterization.

target among different chambers. Figure 2 shows the transfer mechanism of the system. It is composed of one transfer rod, three wobble sticks, three sample manipulators, and the RTTA. In this system, the RTTA, which has a scalable and rotatable arm to move vertically, is the key element which connects the three main functional chambers, i.e., the preparation chamber, the Combi-LMBE chamber, and the STM chamber. Two storage carousels are attached to the end of the transfer rod and the RTTA arm, as shown in the inset of Fig. 2. Each storage carousel can accommodate up to eight sample holders and one target.

All the samples/substrates/tips mounted on the holder can be loaded on the storage carousel from the load-lock chamber and then be further delivered into the preparation chamber by pushing the transfer rod. A wobble stick installed on the preparation chamber is used to move the samples/substrates/tips to the manipulator or the other storage carousel on the RTTA arm. The other two main functional chambers connected to the RTTA chamber have wobble sticks as well. Those wobble sticks fulfill the samples/substrates/tips transfer between the RTTA storage carousel and the manipulator or the STM scanner head. The transfer of the target is straightforward. As shown in the inset of Fig. 2, a fork attached to the front of the storage carousel can carry the target and directly hand it to another fork or the target holder docks on the target stage.

The circumferential arrangement of the three main function chambers around the RTTA chamber presents three advantages: (1) higher space efficiency, making the whole system more compact; (2) higher transfer efficiency so that samples/substrates/tips transfer can be realized between any two chambers; and (3) extensibility, permitting new functional chambers to be easily added to the spare ports of the RTTA chamber.

### C. Sample holder and sample holder dock

Both the sample holder and the sample holder dock designs are critical for this system. Special requirements have been considered for the extended function. First of all, the sample holder should be compatible with other systems so that other *in situ* characterizations

can be done as well. Second, the sample holder should be able to bear a wide temperature range (from liquid helium temperature up to 1000 °C). Third, physical and chemical properties, including thermal and electrical conductivities and chemical stability in the high oxygen environment at high temperature, should be taken into account. Finally, we must position the sample holder precisely in different chambers so that reliable and reproducible data can be obtained.

We have chosen the popular flag-style shape for the sample holder, as shown in Fig. 3(a). The sample holder is made up of Inconel 718 which possesses outstanding physical and chemical properties. Samples or substrates are fixed mechanically by a spring plate in the central square area (10 mm × 10 mm). Three spherical grooves on the back of the sample holder are used to locate the position. The sample holder is inserted into a sample holder dock, as shown in Fig. 3(b). The dock consists of top and bottom plates, and a BeCu spring. Three position balls are pressed into the corresponding holes of the top plate by the BeCu spring. The exposed parts of the balls on the other side of the top plate can be fitted with the spherical grooves on the back of the sample holder for precise positioning.

Considering the functional difference of the sample holder docks in the Combi-LMBE chamber and the STM chamber, we have introduced corresponding alterations, as shown in Figs. 3(c) and 3(d). When we deposit the combi-film, the sample holder needs to be heated up to a high temperature (typically 300–800 °C). The laser as a stable and efficient heater is widely used in deposition systems.<sup>43,44</sup> In order to heat the sample holder and measure the temperature, a 10 mm clearance hole has been made to expose the back surface of the sample holder, and an 808 nm wavelength laser is mounted on the top of the Combi-LMBE chamber and focused on the back of the sample holder with a spot size of 8 mm, as shown in Fig. 3(c). The temperature of the sample holder is measured by using an infrared thermometer, mounted on the Combi-LMBE chamber focusing at an angle of 45°. For the STM sample holder dock [Fig. 3(d)], we embed a diode sensor and a 50 Ω/1 W chip resistor to measure and adjust the sample temperature.

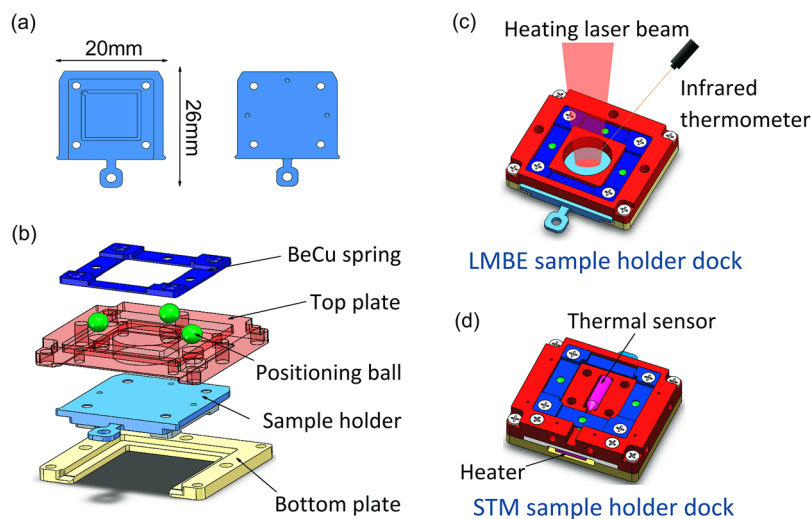


**FIG. 3.** Design of the sample holder. (a) Top and bottom view of the sample holder. (b) Explosion view of the sample holder dock. (c) Sample holder dock for the Combi-LMBE chamber. The red transparent area shows the heating laser optical path. An infrared thermometer focuses on the back of the sample holder at an angle of 45°. (d) Sample holder dock for the STM chamber. The thermal sensor and heater are located in the back and side of sample holder dock, respectively.

## D. Combi-LMBE

The Combi-LMBE chamber is equipped with three customized UHV stages (from UHV design Ltd.), i.e., sample stage, mask stage, and target stage, as shown in Fig. 4(a). The sample stage includes four step-motors for X/Y/Z motions and rotation. The mask stage includes two step-motors for linear motion and mask rotation. A home-made big bowl-shape mask is fixed on the mask stage spindle. The rotary motor possesses a resolution of  $0.02^\circ$ , corresponding to  $40\ \mu\text{m}$  per step, which meets the requirement of combi-film deposition.<sup>45</sup> Above the mask stage, the e-gun of reflection high-energy electron diffraction (RHEED) is mounted aiming at the sample center at an angle of  $2^\circ$  deviation from the sample surface to monitor the film growth *in situ*. The RHEED screen faces the RHEED e-gun to collect the reflected electrons. The target stage includes three step-motors for Z displacement, revolution, and rotation. A 6-seat target holder dock is mounted on the revolution plate. A camera is mounted on the bottom center of the Combi-LMBE chamber for assisting in the alignment of the mask and the sample holder. A 248 nm excimer laser (from Coherent GmbH) at an angle of  $45^\circ$  to the target surface is used to ablate the target material during the deposition.

The typical deposition procedure is illustrated in Fig. 4(b): (i) The mask rotates at a constant speed, and the laser starts to shoot and ablate target A once the right edge of the window in the mask is aligned with the right edge of the substrate, as shown in ①. (ii) The laser stops shooting until the whole substrate is sheltered by the mask, and the first-half period is finished (see ② and ③). (iii) Target B is automatically rotated to the position of target A, and the second-half period starts once the left edge of the window in the mask is aligned with the right edge of the substrate, as shown in ④. (iv) The second-half period is continued until the left edge of the substrate and the left edge of the mask overlap (see ⑤ and ⑥). From steps ① to ③, the A component is deposited with roughly linear distribution from one unit-cell at one end of the substrate to zero coverage at the other end [sketched by the blue triangle in Fig. 4(b)]. After finishing steps ④ to ⑥, the B component is obtained with a reversed thickness distribution compared to the A

component at the same deposition rate and temperature [sketched by the red triangle in Fig. 4(b)]. Thus, we can obtain a unit-cell thin film with a composition continuously varying from A to B. Repeating the above procedure, one can get combi-films of desired thickness, for example, a 100 nm thick (00 $l$ )-oriented (La, Ce)CuO<sub>4</sub> film (the  $c$ -axis lattice constant  $\sim 1.2$  nm) needs more than 80 periods. Following a similar procedure, one can also get thickness-gradient samples or superlattices by controlling the motion sequence of masks and targets using a home-made LabVIEW program.

## E. STM

The STM chamber is equipped with a commercial bath-type cryostat, a double layer cold room, and a home-made scanner. The cryostat consists of two vessels, i.e., a 17 l liquid nitrogen vessel and a 4 l liquid helium vessel. The cold room is mounted at the bottom of the cryostat to isolate from ambient thermal radiation. The STM scanner head is hung inside the 4 K shield by three Inconel springs, which provide vibrational isolation from the cryostat. The total weight of the scanning module is 760 g. The resonant frequency of the suspended scanning module is approximately 2.7 Hz. Eddy current damping is provided by 8 SmCo-magnets mounted on the bottom of the scanner head, as shown in Figs. 5(a) and 5(b). The scanner head is thermal-anchored on a gold-plated oxygenfree high-conductivity copper piece at the bottom of the liquid helium vessel by several copper braids, as shown in Fig. 5(c). The scanner head can be clamped, thereby providing a good stability for transferring tips and samples and a good thermal contact. The details about the cold room, eddy current damping, and scanner clamping mechanism can be found in Ref. 42.

Distinguishing the system from traditional STM systems,<sup>36–39</sup> the closed-loop XY coarse motion of the sample has a large range. Therefore, the tip can be precisely put on the sample surface for determining its physical and chemical properties such as doping level and film thickness. For this, we fixed the STM sample holder dock onto two vertically stacked commercial piezomodules, as shown in Fig. 5(a) (ANPx321-closed loop from Attocube

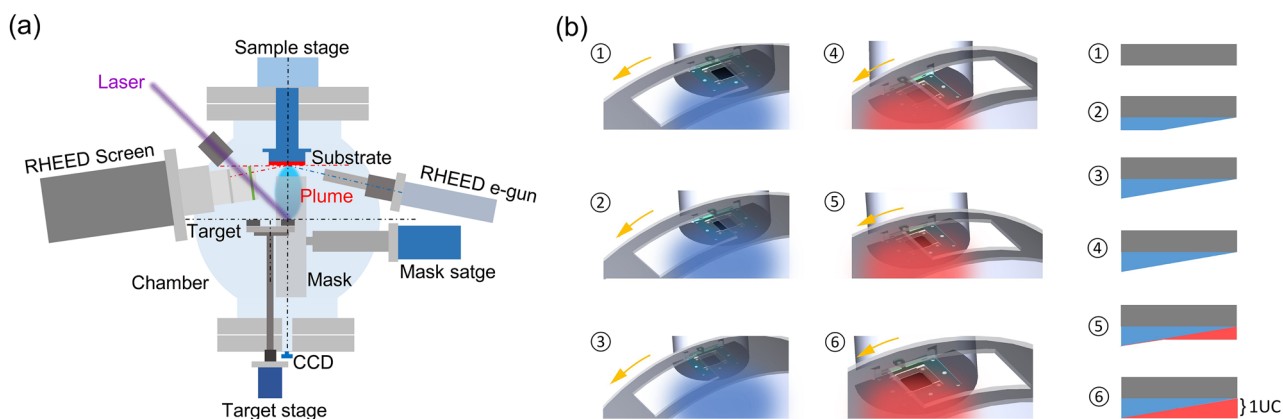


**FIG. 4.** Design of the Combi-LMBE unit and the schematic of the combi-film deposition. (a) Distribution of the main components in the Combi-LMBE chamber. (b) Schematic diagram of the combi-film deposition stages. The left and middle columns show the process of deposition in one cycle. The right column shows the corresponding outcome during sample deposition with the substrate in gray, the component A in blue, and the component B in red.

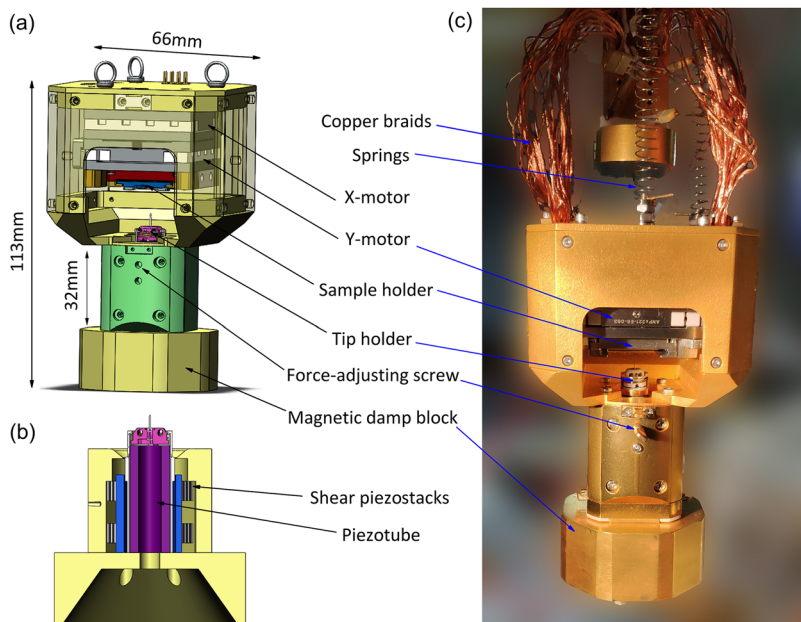


**FIG. 5.** STM scanner head. (a) The 3D model of a homemade scanner head. The sample holder dock is mounted on the X- and Y-motor working in a range of  $15\text{ mm} \times 15\text{ mm}$ . (b) A cross section of the Z-motor. (c) Photograph of the STM scanner head.

system, Inc.). The range of each motor is 15 mm. The fine linear positioning ranges are  $0.8\ \mu\text{m}$  at 4 K and  $5\ \mu\text{m}$  at 300 K, respectively. The lower part of the scanner head is a typical pan-type Z coarse motion with 6 piezostacks, as shown in Fig. 5(b). A simplified inertial tip-approach method is used in this scanner head. More details can be found in Ref. 42.

### III. PERFORMANCE

#### A. Film deposition and characterization

To test the performance of the Combi-LMBE unit, we grew a FeSe thin film with gradient thickness on a LiF substrate. The background vacuum of the chamber was better than  $7.0 \times 10^{-9}$  Torr. The FeSe films were grown with the target-substrate distance of  $\sim 50$  mm,

a laser pulse energy of 350 mJ, a repetition rate of 4 Hz, and the substrate temperature of  $\sim 350^\circ\text{C}$ . Before the deposition, the substrate was aligned with one edge of the window in the mask, as explained in Sec. II D. During the deposition, the mask rotates to gradually shelter the substrate.

The resulting gradient thickness FeSe was then patterned into 10 pieces to perform *ex situ* electrical transport measurements, as shown in the inset of Fig. 6(a). The spatially dependent film thickness, varying from 28 nm to 280 nm as designed, was checked by both x-ray reflection (XRR) and scanning electron microscopy (SEM). All the narrow strips cut from the sample show a sharp superconducting transition, as shown in Fig. 6(a). As the thickness increases, the normal state resistance decreases monotonically as expected. The zero-resistance transition temperatures ( $T_{c0}$ ) of the gradient thickness sample at different regions vary slightly between

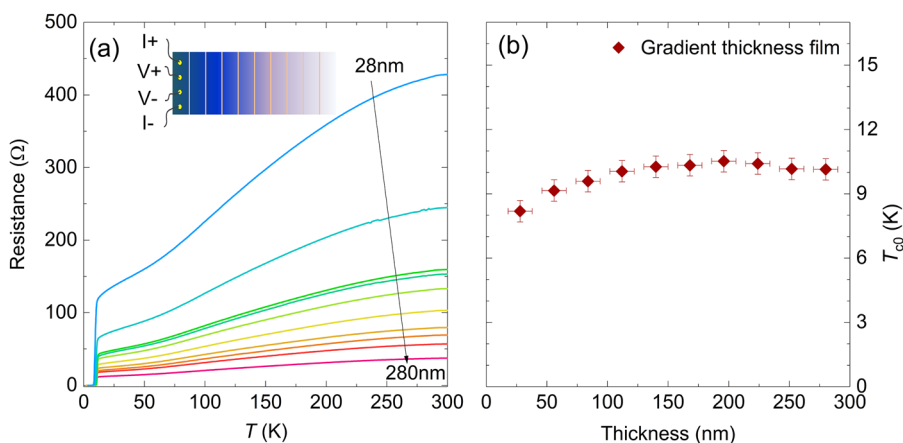


**FIG. 6.** The transport properties of the FeSe film with thickness gradient. (a) Temperature dependence of the resistance of the FeSe film with gradient thickness at different regions. The thickness is the average value at the local region. Inset: electrical transport measurement configuration of the gradient thickness film and orange lines show the dicing of the sample into 10 pieces. (b) Thickness dependence of  $T_{c0}$  for a gradient thickness film.

8 K and 10 K [Fig. 6(b)]. The  $T_{c0}$  values are comparable to those films grown by the conventional pulsed laser deposition (PLD) method in our previous work,<sup>46</sup> verifying that the synthesis part of this system is highly controllable and stable.

## B. STM performance

Before carrying out STM/STS experiments, we tested the low temperature performance of the system. The sample holder in the STM scanner head can be cooled down to  $\sim 5.5$  K in 3 h after the L-He vessel has been precooled with liquid nitrogen. The holding time of liquid helium is around 44 h. The average lateral and vertical drifts of the scanner head are 33 pm/h and 42 pm/h, respectively. The frequency spectra of the background current at room temperature are shown in Fig. 7(a), in the cases of tip retracted and tip approached with feedback turned on or off. The highest peak is lower than  $1 \text{ pA}/\sqrt{\text{Hz}}$  in the situation of tip approached and feedback turned off. These current frequency spectra clearly demonstrate the effective electrical grounding and vibration isolation of the characterization part of our system. To test the location precision of the sample stage, we found an easily identifiable region on the Au (111) surface, as shown in Fig. 7(b). A feature point is marked in the image. Then, the tip is retracted  $0.37 \mu\text{m}$ , and the sample is moved 2 mm along the y-axis and moved back later. The same feature can be observed, as shown in Fig. 7(c). The coordinates of the marked point can be calculated by summing up the feedback values of the Attocube nanopositioner and Nanonis controller. According to the marked

point coordinates before and after moving, the location precision is about  $0.3 \mu\text{m}$ .

The spatial resolution and image quality of our system can be judged from several experiments. A Pt/Ir tip is used for all the tests. We are able to obtain atomic-resolution images of a HOPG cleaved surface at both low temperature and room temperature, as shown in Fig. 8(a). In addition, the herringbone structure and the atomic construction of Au (111) have been clearly resolved after cleaning the sample *in situ* for several cycles by ion gun sputtering and annealing [Fig. 8(b)]. To further verify the stability, we performed STM/STS measurements on a BSCCO single crystal, which is an ideal platform for the test.<sup>35</sup> The sample is cleaved mechanically in the preparation chamber and then transferred to the STM chamber within 5 min. Typical supermodulation images and  $dI/dV$  spectra are shown in Figs. 8(c) and 8(d), respectively. During the differential conductance measurement, the tip position is fixed with the tunneling parameters,  $I_t = 50 \text{ pA}$  and  $V_b = -200 \text{ mV}$ . The amplitude and frequency of the modulation bias are 1 mV and 734 Hz, respectively. From these results, we can estimate a supermodulation period of around 3 nm and a superconducting gap of 44 meV at 77 K, in good agreement with previous reports.<sup>47,48</sup> As a final test, a FeSe film deposited in the Combi-LMBE chamber is transferred into the STM chamber for characterization. The surface topography and atomic resolution images of the FeSe film are shown in Figs. 8(e) and 8(f). The in-plane lattice constant measured from the atomic resolution image is close to the results from XRD measurements ( $a = 3.74 \text{ \AA}$ ).<sup>46</sup>

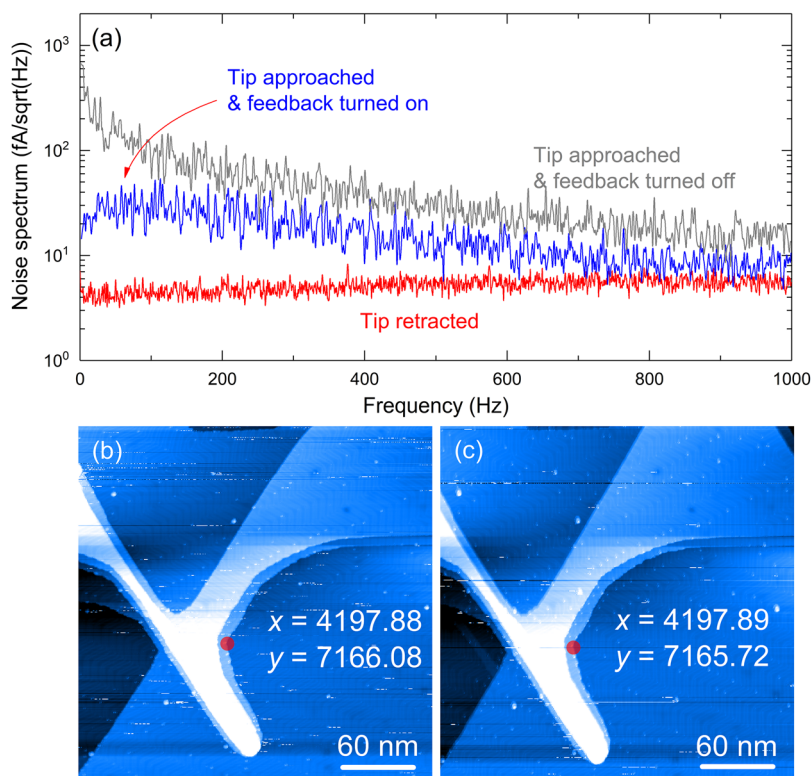


**FIG. 7.** The noise spectra of the tunneling junction and the location precision test. (a) The noise spectra of the background current with the tip retracted (red line), tip approached with feedback turned on (blue line), and the tip approached with feedback turned off (gray line). Before the acquisition of the spectra with the tip approached, the tip is positioned at a fixed height with  $I_t = 0.3 \text{ nA}$  and  $V_b = -0.5 \text{ V}$ . All the spectra are acquired on Au(111) surface at room temperature. [(b) and (c)] The STM images of Au(111) surface at the same region before (b) and after (c) moving the sample away and moving it back. The coordinates with the unit of micrometers are shown in the images. The coordinates of the marked point are calculated by summing up the feedback values of Attocube nanopositioner and Nanonis controller.



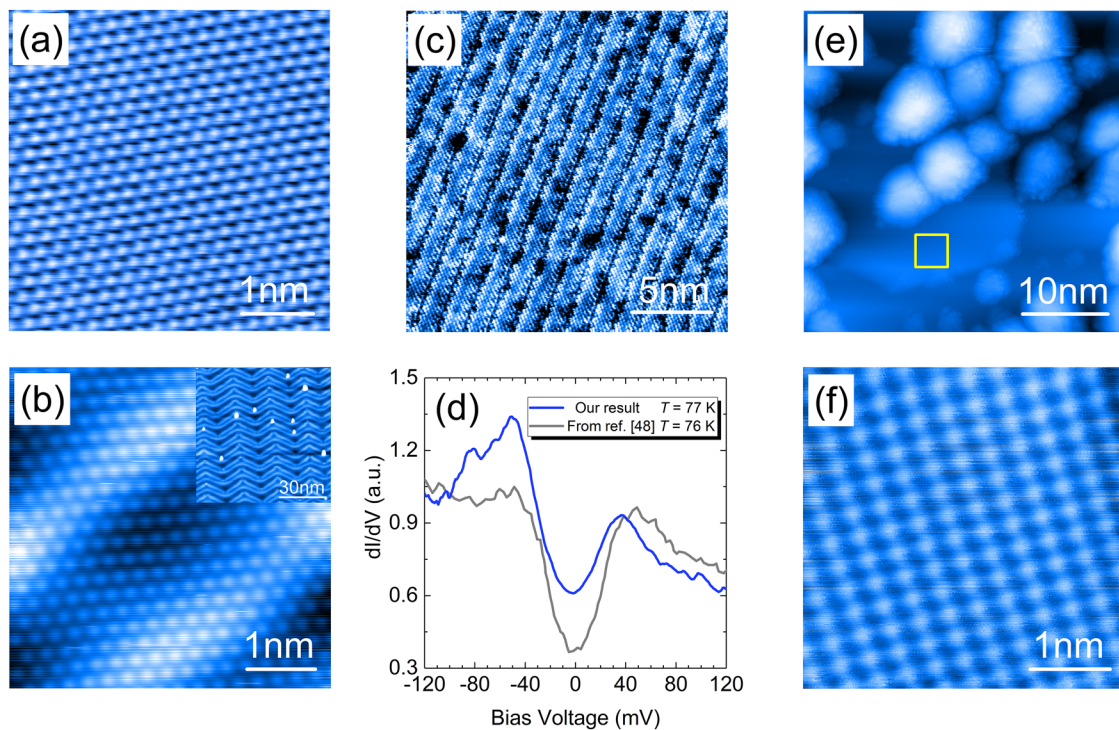


**FIG. 8.** Characterization of STM performance. (a) Atomic construction of the HOPG surface,  $I_t = 0.1$  nA,  $V_b = -0.5$  V, and  $T = 77$  K. (b) Atomic construction of the Au (111) surface,  $I_t = 0.25$  nA,  $V_b = -0.5$  V, and  $T = 5.5$  K. Inset: herringbone reconstruction of the Au (111) surface,  $I_t = 0.1$  nA,  $V_b = -0.5$  V, and  $T = 77$  K. (c) Supermodulation of an *in situ* cleaved clean surface in the BSCCO single crystal,  $I_t = 0.05$  nA,  $V_b = -0.2$  V, and  $T = 5.5$  K. (d)  $dI/dV$  spectrum of the BSCCO single crystal with  $I_t = 0.05$  nA and  $V_b = -0.2$  V (blue line). The amplitude and frequency of the modulation bias are 1 mV and 734 Hz, respectively. The gray  $dI/dV$  spectrum of BSCCO is adapted from Ref. 48. (e) Topographic images of the FeSe thin film surface,  $I_t = 0.1$  nA,  $V_b = -2$  V, and  $T = 77$  K. (f) Atomic construction of the FeSe thin film surface taken from the yellow square region in (e),  $I_t = 0.6$  nA,  $V_b = -0.5$  V, and  $T = 77$  K.

#### IV. CONCLUSION

We report the design, assembly, and performance of an advanced Combi-LMBE-STM facility, intended to accelerate the materials research by integrating high-throughput film synthesis, *in situ* surface morphology, and electronic states characterization. Compared to traditional film deposition techniques, combi-films can be deposited with parameters such as chemical substitution and sample thickness varied continuously in a single run. A rotary mask is used in our system to reduce the accumulative error from conventional reciprocating motion. After the deposition, the samples are transferred to the specially designed STM chamber for *in situ* characterization of surface morphology and electronic states. For compatibility with the combi-film, a large range closed-loop XY coarse positioning module was developed to realize motion in a range of 15 mm  $\times$  15 mm but with submicrometer precision. With this feature, we can measure the evolution of surface morphology and electronic states as a function of the varying parameter (composition or thickness) with high efficiency. The performance of the whole system is demonstrated by the growth of high-quality FeSe film with thickness gradient and topographic images of various samples including HOPG, Au (111), BSCCO single crystal, and FeSe thin film. Clean current noise spectra of the tunneling junction and the  $dI/dV$  spectrum of BSCCO have also been obtained. We expect that this

system will be ideal for a systematic research on superconducting materials.

#### ACKNOWLEDGMENTS

The authors thank Z. B. Wu, Z. Y. Gao, W. H. Wang, X. Y. Hou, R. S. Ma, Y. Li, X. S. Zhu, Professor L. Shan, X. Huang, A. W. Wang, J. H. Yan, X. Y. Chen, Y. Q. Xing, H. Yang, X. C. Huang, H. S. Yu, X. Zhang, W. Hu, Y. L. Jia, Y. J. Shi, X. J. Wei, M. Y. Qin, Z. F. Lin, D. Li, X. Y. Jiang, J. S. Zhang, Z. Y. Zhao, and Q. Li for useful discussions and help. The authors also thank Professor W. A. Hofer, Professor S. X. Du, and Professor A. V. Silhanek for polishing this manuscript. This work was supported by the Scientific Instruments and Equipment Project of the Chinese Academy of Sciences (Grant No. YZ201450), the Special Fund for Research on National Major Research Instruments of NSFC (Grant No. 11927808), CAS Key Technology Research and Development Team Project (Grant No. GJJSTD20170006), the Huairou Science Center of Beijing Municipal Science and Technology Project (Grant No. Z181100003818013), the National Key Basic Research Program of China (Grant Nos. 2015CB921000, 2016YFA0300301, 2017YFA0302902, 2017YFA0303003, and 2018YFB0704102), the National Natural Science Foundation of

China (Grant Nos. 11674374, 11834016, 11804378, 118115301, and 119611410), the Strategic Priority Research Program of Chinese Academy of Sciences (Grant No. XDB25000000), the Key Research Program of Frontier Sciences, CAS (Grant Nos. QYZDB-SSW-SLH008 and QYZDY-SSW-SLH001), and the CAS Interdisciplinary Innovation Team, Beijing Natural Science Foundation (Grant No. Z190008).

## REFERENCES

- <sup>1</sup>P. A. Grunberg, *Rev. Mod. Phys.* **80**, 1531 (2008).
- <sup>2</sup>M. Imada, A. Fujimori, and Y. Tokura, *Rev. Mod. Phys.* **70**, 1039 (1998).
- <sup>3</sup>K. Jin, N. P. Butch, K. Kirshenbaum, J. Paglione, and R. L. Greene, *Nature* **476**, 73 (2011).
- <sup>4</sup>B. Keimer, S. A. Kivelson, M. R. Norman, S. Uchida, and J. Zaanen, *Nature* **518**, 179 (2015).
- <sup>5</sup>L. D. Pham, T. Park, S. Maquilon, J. D. Thompson, and Z. Fisk, *Phys. Rev. Lett.* **97**, 056404 (2006).
- <sup>6</sup>F. Kretschmar, T. Bohm, U. Karahasanovic, B. Muschler, A. Baum, D. Jost, J. Schmalian, S. Caprara, M. Grilli, C. Di Castro, J. G. Analytis, J. H. Chu, I. R. Fisher, and R. Hackl, *Nat. Phys.* **12**, 560 (2016).
- <sup>7</sup>M. Vojta, *Rep. Prog. Phys.* **66**, 2069 (2003).
- <sup>8</sup>S. Sachdev, *Physica C* **470**, S4 (2010).
- <sup>9</sup>N. P. Butch, K. Jin, K. Kirshenbaum, R. L. Greene, and J. Paglione, *Proc. Natl. Acad. Sci. U. S. A.* **109**, 8440 (2012).
- <sup>10</sup>J. J. Hanak, *J. Mater. Sci.* **5**, 964 (1970).
- <sup>11</sup>K. Jin, R. Suchoski, S. Fackler, Y. Zhang, X. Q. Pan, R. L. Greene, and I. Takeuchi, *APL Mater.* **1**, 042101 (2013).
- <sup>12</sup>J. Wu, O. Pelleg, G. Logvenov, A. T. Bollinger, Y. J. Sun, G. S. Boebinger, M. Vanevic, Z. Radovic, and I. Bozovic, *Nat. Mater.* **12**, 877 (2013).
- <sup>13</sup>H. Koinuma and I. Takeuchi, *Nat. Mater.* **3**, 429 (2004).
- <sup>14</sup>K. Kennedy, T. Stefansk, G. Davy, V. F. Zackay, and E. R. Parker, *J. Appl. Phys.* **36**, 3808 (1965).
- <sup>15</sup>X. D. Xiang, X. D. Sun, G. Briceno, Y. L. Lou, K. A. Wang, H. Y. Chang, W. G. Wallacefreedman, S. W. Chen, and P. G. Schultz, *Science* **268**, 1738 (1995).
- <sup>16</sup>Z. L. Luo, B. Geng, J. Bao, and C. Gao, *J. Comb. Chem.* **7**, 942 (2005).
- <sup>17</sup>P. Ahmet, Y. Z. Yoo, K. Hasegawa, H. Koinuma, and T. Chikyow, *Appl. Phys. A: Mater. Sci. Process.* **79**, 837 (2004).
- <sup>18</sup>M. Murakami, K. S. Chang, M. A. Aronova, C. L. Lin, M. H. Yu, J. H. Simpers, M. Wuttig, I. Takeuchi, C. Gao, B. Hu, S. E. Lofland, L. A. Knauss, and L. A. Bendersky, *Appl. Phys. Lett.* **87**, 112901 (2005).
- <sup>19</sup>T. Byrne, L. Lohstreter, M. J. Filiaggi, Z. Bai, and J. R. Dahn, *Surf. Sci.* **602**, 2927 (2008).
- <sup>20</sup>J. E. Daniels, W. Jo, J. Rodel, V. Honkimaki, and J. L. Jones, *Acta Mater.* **58**, 2103 (2010).
- <sup>21</sup>J. L. Jones, A. Pramanick, and J. E. Daniels, *Appl. Phys. Lett.* **93**, 152904 (2008).
- <sup>22</sup>Z. L. Luo, B. Geng, J. Bao, C. H. Liu, W. H. Liu, C. Gao, Z. G. Liu, and X. L. Ding, *Rev. Sci. Instrum.* **76**, 095105 (2005).
- <sup>23</sup>J. S. Wang, Y. Yoo, C. Gao, I. Takeuchi, X. D. Sun, H. Y. Chang, X. D. Xiang, and P. G. Schultz, *Science* **279**, 1712 (1998).
- <sup>24</sup>Z. W. Jin, T. Fukumura, M. Kawasaki, K. Ando, H. Saito, T. Sekiguchi, Y. Z. Yoo, M. Murakami, Y. Matsumoto, T. Hasegawa, and H. Koinuma, *Appl. Phys. Lett.* **78**, 3824 (2001).
- <sup>25</sup>Y. Matsumoto, M. Murakami, T. Shono, T. Hasegawa, T. Fukumura, M. Kawasaki, P. Ahmet, T. Chikyow, S. Koshihara, and H. Koinuma, *Science* **291**, 854 (2001).
- <sup>26</sup>P. J. Curran, H. A. Mohammed, S. J. Bending, A. E. Koshelev, Y. Tsuchiya, and T. Tamegai, *Sci. Rep.* **8**, 10914 (2018).
- <sup>27</sup>A. M. Chang, H. D. Hallen, L. Harriott, H. F. Hess, H. L. Kao, J. Kwo, R. E. Miller, R. Wolfe, J. Vanderziel, and T. Y. Chang, *Appl. Phys. Lett.* **61**, 1974 (1992).
- <sup>28</sup>T. Wei, X. D. Xiang, W. G. Wallacefreedman, and P. G. Schultz, *Appl. Phys. Lett.* **68**, 3506 (1996).
- <sup>29</sup>K. Hasegawa, P. Ahmet, N. Okazaki, T. Hasegawa, K. Fujimoto, M. Watanabe, T. Chikyow, and H. Koinuma, *Appl. Surf. Sci.* **223**, 229 (2004).
- <sup>30</sup>K. Lai, M. B. Ji, N. Leindecker, M. A. Kelly, and Z. X. Shen, *Rev. Sci. Instrum.* **78**, 063702 (2007).
- <sup>31</sup>K. C. Hewitt, P. A. Casey, R. J. Sanderson, M. A. White, and R. Sun, *Rev. Sci. Instrum.* **76**, 093906 (2005).
- <sup>32</sup>B. C. Stipe, M. A. Rezaei, and W. Ho, *Science* **280**, 1732 (1998).
- <sup>33</sup>A. J. Heinrich, J. A. Gupta, C. P. Lutz, and D. M. Eigler, *Science* **306**, 466 (2004).
- <sup>34</sup>V. Madhavan, W. Chen, T. Jamneala, M. F. Crommie, and N. S. Wingreen, *Science* **280**, 567 (1998).
- <sup>35</sup>Ø. Fischer, M. Kugler, I. Maggio-Aprile, C. Berthod, and C. Renner, *Rev. Mod. Phys.* **79**, 353 (2007).
- <sup>36</sup>J. D. Hackley, D. A. Kisilitsyn, D. K. Beaman, S. Ulrich, and G. V. Nazin, *Rev. Sci. Instrum.* **85**, 103704 (2014).
- <sup>37</sup>B. C. Stipe, M. A. Rezaei, and W. Ho, *Rev. Sci. Instrum.* **70**, 137 (1999).
- <sup>38</sup>J. W. Lyding, S. Skala, J. S. Hubacek, R. Brockenbrough, and G. Gammie, *Rev. Sci. Instrum.* **59**, 1897 (1988).
- <sup>39</sup>G. Meyer, *Rev. Sci. Instrum.* **67**, 2960 (1996).
- <sup>40</sup>B. G. Orr, C. W. Snyder, and M. Johnson, *Rev. Sci. Instrum.* **62**, 1400 (1991).
- <sup>41</sup>W. Z. Lin, A. Foley, K. Alam, K. K. Wang, Y. H. Liu, T. J. Chen, J. Pak, and A. R. Smith, *Rev. Sci. Instrum.* **85**, 043702 (2014).
- <sup>42</sup>Z. B. Wu, Z. Y. Gao, X. Y. Chen, Y. Q. Xing, H. Yang, G. Li, R. S. Ma, A. W. Wang, J. H. Yan, C. M. Shen, S. X. Du, Q. Huan, and H. J. Gao, *Rev. Sci. Instrum.* **89**, 113705 (2018).
- <sup>43</sup>P. E. Dyer, A. Issa, P. H. Key, and P. Monk, *Supercond. Sci. Technol.* **3**, 472 (1990).
- <sup>44</sup>R. C. Estler, N. S. Nogar, R. E. Muenchausen, X. D. Wu, S. Foltyn, and A. R. Garcia, *Rev. Sci. Instrum.* **62**, 437 (1991).
- <sup>45</sup>H. S. Yu, J. Yuan, B. Y. Zhu, and K. Jin, *Sci. China: Phys., Mech. Astron.* **60**, 087421 (2017).
- <sup>46</sup>Z. P. Feng, J. Yuan, G. He, W. Hu, Z. F. Lin, D. Li, X. Y. Jiang, Y. L. Huang, S. L. Ni, J. Li, B. Y. Zhu, X. L. Dong, F. Zhou, H. B. Wang, Z. X. Zhao, and K. Jin, *Sci. Rep.* **8**, 4039 (2018).
- <sup>47</sup>S. H. Pan, J. P. O'Neal, R. L. Badzey, C. Chamon, H. Ding, J. R. Engelbrecht, Z. Wang, H. Eisaki, S. Uchida, A. K. Gupta, K. W. Ng, E. W. Hudson, K. M. Lang, and J. C. Davis, *Nature* **413**, 282 (2001).
- <sup>48</sup>C. Renner, B. Revaz, J. Y. Genoud, K. Kadowaki, and O. Fischer, *Phys. Rev. Lett.* **80**, 149 (1998).